Magnetic Nested-wind Scenarios for Bipolar Outflows: Pre-planetary and YSO nebular shaping [1]

Timothy J. Dennis[1], Adam Frank[1], Eric G. Blackman[1]

Orsola DeMarco[2,5], Bruce Balick[3]

and

Sorin Mitran[4]

ABSTRACT

We present results of a series of magnetohydrodynamic (MHD) and hydro-dynamic (HD) 2.5D simulations of the morphology of outflows driven by nested wide-angle winds - i.e. winds which eminate from a central star as well as from an orbiting accretion disk. While our results are broadly relevent to nested wind systems we have tuned the parameters of the simulations to touch on issues in both Young Stellar Objects and Planetary Nebula studies. In particular our studies connect to open issues in the early evolution of Planetary Nebulae. We find that nested MHD winds exhibit marked morphological differences from the single MHD wind case along both dimensions of the flow. Nested HD winds on the other hand give rise mainly to geometric distortions of an outflow that is topologically similar to the flow arising from a single stellar HD wind. Our MHD results are insensitive to changes in ambient temperature between ionized and un-ionized circumstellar environments. The results are sensitive to the relative mass-loss rates, and to the relative speeds of the stellar and disk winds. We also present synthetic emission maps of both nested MHD and HD simulations. We find that nested MHD winds show knots of emission appearing on-axis that do not appear in the HD case.

[1]Department of Physics & Astronomy, University of Rochester, Rochester, NY 14627; tdennis@pas.rochester.edu

[2] Department of Astrophysics, American Museum of Natural History, Central Park West at 79th Street, New York, NY 10024

[3]Department of Astronomy, University of Washington, Seattle, WA 98195

[4] Department of Mathematics, University of North Carolina, Chapel Hill, NC 27599

[5]Department of Physics, Macquaurie University, Sydney NSW 2109, Australia

Subject headings: ISM:jets and outflows—planetary nebulae:general—stars:AGB and Post-AGB

1. Introduction

Starting in 1994, the Hubble Space Telescope (HST) began returning images with unprecedented detail of what were thought to be familiar and well-understood objects. The images made it clear that the so-called Generalized Interacting Stellar Winds (GISW) model was inadequate to explain the morphologies of several classes of Planetary Nebulae (PN's) and Proto-Planetary Nebulae (PPN's) (Balick & Frank 2002). In particular the narrow-wasted bipolar, multipolar, and point-symmetric classes could not be explained as being solely due to the interaction of an isotropic fast wind with the material previously deposited by the slow, "superwind" phase of AGB mass-loss; even when accounting for the ubiquitous presence of dense, dusty disks or tori surrounding the central post-AGB star first observed by Balick (1987). In addition, a number of smaller-scale, low-ionization, observational features associated with approximately half of known PN's in the form of knots, collimated jet-like structures, and the remarkable "Fast Low-Ionization Emission Regions" (FLIERS) indicate that there is much that remains to be understood about the physics occurring in these environments (Gonçalves et al. 2001).

An $H\alpha$ HST survey of very young PN's carried out by Sahai & Trauger (1998) revealed the presence of bipolar ansae and/or collimated radial structures indicating the presence of jets. In others, bright structures in proximity to the minor axes were observed, indicative of the disks and tori mentioned previously. Sahai & Trauger (1998) proposed that high-speed collimated jets serve as the primary agent of the shaping process. Later theoretical work by Soker & Rappaport 2000 and Soker 2004 entensively explored the ability of collimated hydrodynamic winds to shape PN. Numerical work on this model has been carried out in a series of revealing studies by Lee & Sahai (2003, 2004, 2009) and Akashi & Soker (2008)

The presence of both disks and jet-like structures is reminiscent of the enviroments of Young Stellar Objects (YSO's), where jets drive ubiquitous molecular outflows. YSO jets are believed to be magnetically launched and these mechanisms for driving the outflows have been extensively studied (Blandford & Payne 1982, Pudritz & Norman 1983, Uchida &

Shibata 1985, Shu et al. 1988, Contopoulis & Lovelace 1994, Shu et al. 1994a,b, Goodson & Winglee 1999). This led some to speculate that jets in PN's and PPN's may also be magnetically driven (Blackman et al. 2001a, 2001b; Frank & Blackman 2004; Matt et al. 2006; Frank 2006). Some indirect support for MHD driving in PN's is provided by the observations of Bujarrabal et al. (2001) who, in a survey of 37 PPN's, found fast winds associated with 28 of these objects with momenta that are in most cases too high—sometimes by a factor of 10^3—to be accounted for by radiation pressure.

Blackman et al. (2001a) have shown that a dynamo operating in an AGB star can produce magnetic fields powerful enough to drive a self-collimating outflow accounting at once for both the momentum problem and the observed collimation. The means by which the field so generated drives and collimates the outflow is presumed to be the "magnetocentrifugal launch" mechanism (MCL) (Blandford & Payne 1982, Pelletier & Pudritz 1992). Because such a dynamo operating in an isolated star is subject to the criticism that some mechanism for restoring shear is necessary in order to maintain it, more recent work has focused on common-envelope dynamos in which the rotational energy needed to maintain the dynamo is supplied by an embedded low-mass companion. Nordhaus et al. (2007) have recently shown that for a variety of such scenarios a robust dynamo results.

In the MCL scenario for disk-winds, a poloidal field threading the disk and sufficiently inclined with respect to the disk axis, acts as a conduit for coronal gas experiencing centrifugal forces that overbalance gravitational attraction. The material is thus "flung" out along the poloidal lines of force, until it passes beyond the "Alfvèn surface", where magnetic tension is no longer sufficient to maintain co-rotation of the field resulting in shear and the consequent development of a toroidal component which ultimately dominates at sufficiently large distances. The toroidal field is buoyant and thus "rises" through the radially stratified circumstellar environment carrying the disk material with it while simultaneously ensuring a high degree of collimation of the material it carries because of the field's hoop stress.

It has additionally been pointed out that the MCL scenario can occur more impulsively even in the absence of disks when linked to the rapid evolution of the source of the field. The driver in this case would be stellar differential rotation and the consequent shearing of a stellar magnetic field in the ionized circumstellar environment. Such a mechanism may apply to gamma-ray bursts or supernovae (e.g. Piran 2005), and has been examined both analytically and numerically by a number of authors (Klužniak & Ruderman 1998; Wheeler et al. 2002; Akiyama et al. 2003; Blackman et al. 2006). The added presence of disks in the environments of post-AGB stars, together with the presumption of the presence of magnetic fields in both, have led us to consider the possibility that not one, but two "fast" $(10^2 - 10^3$ km s$^{-1})$ magnetic winds may be operating simultaneously in the enviroments of at

least some post-AGB objects. In such a scenario it is likely that the spherical symmetry of the stellar-wind source will result in a broader opening angle than that of the disk-wind that surrounds it, leading to a collision of the two winds occurring relatively near their sources. Such an interaction, if it occurs, is very likely to have a profound influence on the ensuing morphological development of the shock-heated emitting structures thereby manifested.

Rożyczka & Franco (1996) were the first to present simulations showing that a diverging fast-wind, threaded by a toroidal magnetic field, and incident upon an unmagnetized ambient medium modeled to be consistent with environments observed around evolved stars, can collimate the wind provided the magnetic field is sufficiently strong. Soon after, Frank et al. (1998) presented a set of axially symmetric magnetohydrodynamic (MHD) simulations examining the influence of strong magnetism on the morphological and kinematical features of radiative jets in the context of YSO's, and found that they differ significantly from corresponding hydrodynamic (HD) and weak field cases, forming "nose-cones" at the head of the jet, narrower bow shocks, and enhanced bow shock speeds. These effects were attributed to the hoop stresses imposed upon the flow by the toroidal field. In subsequent work, Frank et al. (2000) added greater realism by using analytical models of MCL launching to specify the cross-sectional distributions of the jet's state variables. The resulting radial stratification of density and magnetic field led to new propagation behavior manifested principally by the development of an inner jet core within a lower density collar. Several studies of both pulsed and steady radiative jets have addressed the effect of various magnetic field topologies on the emission features of jets (Stone & Hardee, 2000; O'Sullivan & Ray, 2000; Cerqueira & de Gouveia Dal Pino 1999, 2001a,b; de Gouveia Dal Pino & Cerqueira 2002). It is found that the emission structures resulting from the imposition of helical or toroidal field configurations depart the most from their purely hydrodynamic analogs, but that the differences that arise become less pronounced, and in the case of the nose cones, even vanish in fully three dimensional calculations (Cerqueira & de Gouveia Dal Pino 1999, 2001a,b). De Colle & Raga (2006) have studied the Hα emission of axisymmetric radiative jets threaded with toroidal fields and have concluded that the greater jet collimation leads to an increase in Hα emission along the jet axis, and, like Frank et al. (1998), a somewhat increased shock velocity relative to the hydrodynamic case.

The possibility of contemporaneous disk and stellar winds is not restricted to PN's and PPN's. Evidence exists for this phenomenon in every environment where jets and accretion disks are found (see, e.g. Livio 1997 and references therein). Nonetheless most studies of magnetized winds focus on individual jets and do not address the question of how simultaneously operating stellar and disk winds may interact with one another as evidenced by the brief survey of literature provided above. The relatively few studies involving simultaneous outflows include those of Meliani et al. (2006) and Casse et al. (2007), who examined the

launch physics of simultaneous outflows in the YSO context using non-ideal MHD simulations for a self-consistent accounting of the viscous and resistive accretion disk, of Matsakos et al. (2008), who studied the topological stability of two-component outflows for a pair of prototypical and complementary analytical solutions via time-dependent MHD simulations, and of Fendt (2008), who addressed the question of how the formation of large-scale jets is affected by the interaction of the central stellar magnetosphere and stellar wind with a surrounding magnetized disk outflow using axisymmetric MHD simulations.

In the context of PN's, the ability of collimated winds to produce the diverse features seen in many collimated PN's has been studied in some detail in the hydrodynamic case by Akashi (2007), Akashi & Soker (2008) and Akashi et al (2008). In these studies a wide angle wind ($\theta > 10^o$) from a central source was ejected into a spherical AGB wind. The evolution of the subsequent nebula was tracked to observable scales. The authors showed that the resulting morphology could recover a number of important features seen in real PN's such as front lobes and rings on the main bipolar structure. Of particular importance were the equatorial rings formed as wind-angle winds/jets would lead to compression of material in the symmetry plane (which is expected to be both the plane of the disk and the plane of the binary orbit. These studies were important in their ability to demonstrate the range of features which could be produced via wide angle jets.

We are presently unaware of any previous numerical study examining the macroscopic features of the resulting flow and environment for two simultaneously flowing, nested winds. The purpose of the present work is to examine the morphological consequences of pairs of simultaneous, steady, radiative, toroidally magnetized, and nested winds, and to compare the results of these simulations to similar winds for which the magnetic field and/or the disk wind is absent.

The remainder of this paper is structured as follows: section 2 presents a description of the simulations performed, detailing the boundary conditions used for the wind-launching region, the parameters chosen to characterize the winds, the ambient environment into which they flow, the nature of the magnetic field imposed and the initial conditions for each simulation presented. In section 3 we present graphical comparisons among the various simulations and our description and interpretation of the structures observed. In section 4 we present our conclusions.

2. Numerical Model

2.1. Geometry

We execute a series of axisymmetric, radiatively cooled simulations of two co-axial, or "nested," magnetohydrodynamic (MHD), and hydrodynamic (HD) winds flowing simultaneously into a rectangular domain from a source located at the lower left boundary. The long (z) axis is chosen to correspond to a physical size equal to 2×10^4 AU while the short (r) axis is 8×10^3 AU. The direction of flow is predominantly along z. A diagram of the boundary condition assumed in the region where the winds are launched is shown in figure 1. Two radii, r_d and r_s, are defined to delineate the regions where the inner "stellar" wind and the outer "disk" wind operate. In the range $r < r_\mathrm{s}$ of the launch region, the parameters specifying the stellar wind determine the properties of the flow there, while for $r_\mathrm{s} < r < r_\mathrm{d}$ the flow properties are determined by the parameters specifying the disk wind. The parameters chosen to specify the winds include the disk-wind and stellar-wind mass-loss rates; $\dot{M}_\mathrm{d}$, and $\dot{M}_\mathrm{s}$; their velocities; v_d and v_s; their opening angles; θ_d and θ_s, and two dimensionless parameters β_m, and σ to be discussed below. As indicated in figure 1 the wind opening angles are upper limits on the degree to which the flow directions depart from being parallel with the z-axis. For a cell in the launch region a distance r from the origin, the velocity vector for the flow emerging from that element makes an angle $(r/r_\mathrm{w})\theta_\mathrm{w}$ with respect to the z-axis, where θ_w is one of θ_s or θ_d, and where r_w is one of r_s or r_d depending on whether $r < r_\mathrm{s}$ or $r > r_\mathrm{s}$ respectively. The opening angles are both non-zero with the disk-wind opening angle shallower than that of the stellar wind. The intent is to choose opening angles here that accord with the notion that the disk wind is launched magnetocentrifically and "flung" out along poloidal field lines while the stellar wind mass loss is more nearly isotropic. The angles chosen for the simulations presented here represent our best effort to model this scenario while respecting the technical limitations imposed upon us by the code.

2.2. Parameterization

Throughout the launch region, at each time-step, a toroidal magnetic field is embedded in the winds. To characterize the strength and dynamical significance of this field we introduce the independent parameters σ and β_m, where σ is the ratio of wind magnetic energy density to wind kinetic energy or,

$$\sigma = \frac{B^2/8\pi}{\rho_\mathrm{w} v_\mathrm{w}^2}, \tag{1}$$

and β_{m} is a particular value of the ratio of thermal pressure to magnetic pressure, chosen to be characteristic of the wind, i.e.,

$$\beta_{\mathrm{m}} = 8\pi P_{\mathrm{w}}/B_{\mathrm{m}}^2, \tag{2}$$

where B_{m} is a maximum value for the magnetic field strength. By specifying the values of σ and β, and constraining the value of wind mass density, ρ_{w}, by requiring a relation of the form

$$\dot{M} = \Omega \rho_{\mathrm{w}} v_{\mathrm{w}} r_{\mathrm{w}}^2 \tag{3}$$

(where Ω is the solid angle of the wind) to hold among the mass-loss rates, velocities, and radii of the stellar and disk winds [2], we infer a characteristic value for the thermal pressure of the wind P_{w} by way of the relation

$$P_{\mathrm{w}} = \rho_w v_{\mathrm{w}}^2 \sigma \beta, \tag{4}$$

and fix the value of B_{m}, from the definition of β_{m}. I.e.,

$$B_{\mathrm{m}} = \sqrt{8\pi P_{\mathrm{w}}/\beta_{\mathrm{m}}}. \tag{5}$$

Finally, using the values of P_{w} and B_{m} thus obtained we model the magnetic and pressure profiles, $B(r)$ and $P(r)$ for the winds after the form first introduced by Lind et al. (1989). For the magnetic field profile we write:

$$B(r) = \begin{cases} B_{\mathrm{m}}\frac{r}{r_{\mathrm{m}}}, & 0 \le r < r_{\mathrm{m}} \\ B_{\mathrm{m}}\frac{r_{\mathrm{m}}}{r}, & r_{\mathrm{m}} \le r < r_{\mathrm{d}} \\ 0, & r \ge r_{\mathrm{d}} \end{cases} \tag{6}$$

and for the pressure profile we write:

$$P(r) = \begin{cases} \left[\alpha + \frac{2}{\beta_{\mathrm{m}}}\left(1 - \frac{r^2}{r_{\mathrm{m}}^2}\right)\right] P_{\mathrm{w}}, & 0 \le r < r_{\mathrm{m}} \\ \alpha P_{\mathrm{w}}, & r_{\mathrm{m}} \le r < r_{\mathrm{d}} \\ P_{\mathrm{w}}, & r \ge r_{\mathrm{d}} \end{cases} \tag{7}$$

The quantity α is a constant related to β_{m} according to:

$$\beta_{\mathrm{m}}^{-1} = (1 - \alpha)(r_{\mathrm{d}}/r_{\mathrm{m}})^2, \tag{8}$$

and r_{m} is the value of r at which $B = B_{\mathrm{m}}$, and is chosen in all of the simulations presented here to be equal to the "stellar" radius r_{s}. One may verify that with the profiles defined as in

---

[2]for the disk wind we require $r_{\mathrm{w}}^2 = r_{\mathrm{d}}^2 - r_{\mathrm{s}}^2$

equations (6) and (7) the pressure and magnetic field satisfy the condition of magnetostatic equilibrium, i.e.,

$$\frac{dP}{dr} = -\frac{B}{4\pi r}\frac{d(rB)}{dr},$$

(9)

everywhere in the interior of the winds except at $r = r_{\mathrm{m}}$ where the value of P_{w} (and therefore B_{m}) changes. The winds are launched into a homogeneous, unmagnetized ambient medium whose total number density, n_{a}, and temperature T_{a} are chosen independently. As a consequence, the winds are not pressure-matched with respect to their environment in the simulations. We allow this freedom so that we may explore how shaping is affected by changes in the circum-stellar environment (see section 3.3).

Lastly we note that since all of the parameters σ, β_{m}, $\dot{M}_{\mathrm{s}}$, $\dot{M}_{\mathrm{d}}$, v_{d}, v_{s}, r_{d}, and r_{s} are set independently, the simulations are not controlled with respect to the total power in the winds. However, because the field strength in the winds has been kept relatively low, the magnetic contribution to the outflow power, $\mathcal{P}_{\mathrm{B}}$, is small ($\mathcal{P}_{\mathrm{B}} \lesssim \sigma\mathcal{P}_{\mathrm{tot}}$) in all of the simulations presented, facilitating the comparisons below and arguing against the possibility that the differences seen between the MHD and HD runs are the result of a dominant energy effect.

2.3. Methods and initial conditions

We have executed nine, radiatively cooled, axially-symmetric simulations using "AstroBEAR." AstroBEAR is an AMR Hydro/MHD code based on the conservative form of the MHD equations and designed for use with high-resolution shock capturing methods for sets of nonlinear hyperbolic equations. We use AstroBEAR to solve either the ideal MHD equations for the magnetized winds, or the equations of inviscid hydrodynamics (i.e. the Euler equations) for the unmagnetized winds. In both cases we assume that the field variables do not depend on the azimuthal angle so that our solutions are axially-symmetric. This allows us to reduce the problem to a 2-dimensional calculation. Because the solutions that result represent "slices" through the axis of symmetry of the full 3-dimensional axisymmetric solution, they are said to be 2.5-dimensional (2.5D). For a description of AstroBEAR and the equation set it solves see Cunningham, et al. (2008).

Short descriptions of each simulation and their parameterizations are given in table's 1 and 2. Table 1 lists the values of those parameters which are common to all cases, and table 2 lists each run and its corresponding parameterization. All but one of these simulations was carried out on a grid of base resolution 640×256 and with two levels of refinement for an effective resolution 2560×1024. One simulation (run A2) was carried out on a fixed grid of

resolution 2560×1024. In every case the discretization used corresponds to a resolution of 64 cells per disk-wind radius, or 16 cells per stellar-wind radius. The standard case, in which two MHD winds interact as suggested by figure 1, is presented as run A1. For purposes of comparison, we also present a hydrodynamic case, cases for which the outermost of the two winds is absent, and cases for which the stellar wind is "lighter" than the disk wind, (i.e., the stellar mass-loss rate is an order of magnitude smaller). Two further cases are also presented for nested HD and MHD winds in order to compare the morphologies obtained in a warm ($\sim 10^4$ K) circumstellar environment to those obtained in a cool ($\sim 10^2$ K) environment.

The domain of computation is scaled so that one computational unit of length corresponds to 500 AU. The physical size of the domain thus corresponds to a length along z of 2×10^4 AU and a length along r of 8×10^3 AU. The simulations are each run for the length of time required for the flow to reach the right end of the domain. These times are given in physical units in table 2.

We note that the use of a constant density ambient medium was a response to our desire to make the simulations as general as possible allowing these models to address issues relevent to both YSO jets, PNe and other disk/central source systems. Not including a $1/r^2$ density fall off appropriate to the AGB wind will affect the results in terms of timescales (as the winds/jets will see lower momentum densities in the ambient medium as they propogate outwards). If the AGB wind is spherically symmetric on nebular scales we do not, however, expect dramatic changes in morphology. This point can be explored in further studies which are beyond the scope of the current work. We note some aspects of this problem have been covered by Akashi 2007, and Akashi & Soker 2008 for the nonmagnetic case.

We note also that the velocity scales are chosen to be appropriate for either YSOs (a wind from the inner edge of a disk) or the preplanetary nebular phase. For the preplanetary case we take this speed to be indicative of the bridge between the AGB wind (10 km/s) and the circumstellar wind (1000 km/s). In addition we note that we are interested in the long term of evolution of the morphology and so we have had to make certain choices based on computational expediency and our desire to provide simulations that are generally relevent to nested wind systems. Thus the size scale of the disk boundary condition is larger than should be expected in some systems. Future studies will be needed to connect behavior at the smallest scales where the disk winds are launched and disk and stellar winds interact (Garcia- Arrendondo & Frank 2006) and the largest scales where full nebular morphology has been been established.

While our initial ambient temperature is appropriate for mature PNe (see Akashi & Soker 2008) it is too high for PPN and YSOs except irradiated YSO jets where $T = 10^4 K$ is a reasonable choice for the ambient medium. As we shall demonstrate however in the case

of MHD winds, which are our principle concern, the choice of the ambient temperature is not a significant factor in the determining the morphology. We have included a discussion early in the paper on the distiction between YSO and PN temperatures.

We use relatively wide jets ($\theta > 10°$) in our simulations. The presence of such a wide jets or wide-angle winds has been conjectured for some in time in YSO systems (Shu et al 1994) and can be seen as a diagnostic for launch mechanisms. In PN systems Soker 2004 has presented analytical arguments for the existence of such wide winds/jets. Such wide outflow systems are likely to be important for creating wider lobes in the observed nebulae in both classes of bipolar nebulae (YSO and PN) .

In all cases, optically-thin, atomic line cooling based upon the cooling curve of Dalgarno and McCray (1972) is assumed. A temperature "floor," $T_{\rm f} = 9.0 \times 10^3$, is set so that only material heated to temperatures $T \geq T_{\rm f}$ is subject to radiative energy loss. No attempt is made to follow the ionization dynamics of the flow. Note that adiabatic cooling continues to operate below the floor for radiative cooling. Because our focus in this paper is restricted to the morphological features that arise from the interaction of nested winds, and from their interaction with their common environment, this approximation is not expected to materially affect our conclusions.

Effective Resolution	16 cells/$r_{\rm s}$
σ	0.1
β	1.0
$n_{\rm a}$	5×10^3 cm^{-3}
$\theta_{\rm s}$	30°
$\theta_{\rm d}$	15°
$r_{\rm s}$	125 AU
$r_{\rm d}$	500 AU

Table 1: Parameters common to all simulations

Run	Description	$\dot{M}_{\rm s}$ (M$_\odot$ yr^{-1})	$\dot{M}_{\rm d}$ (M$_\odot$ yr^{-1})	$v_{\rm s}$ (km s^{-1})	$v_{\rm d}$ (km s^{-1})	$T_{\rm a}$ (K)	run time (10^3 yr)
A1	MHD, both winds on	10^{-7}	10^{-7}	150	50	10^4	1.3
B1	HD, both winds on	10^{-7}	10^{-7}	150	50	10^4	3.1
A2	MHD, disk wind off	10^{-7}	0	150	0	10^4	0.9
B2	HD, disk wind off	10^{-7}	0	150	0	10^4	3.0
A3	cool MHD, both winds on	10^{-7}	10^{-7}	150	50	10^2	1.3
B3	cool HD, both winds on	10^{-7}	10^{-7}	150	50	10^2	3.9
A4	MHD, light stellar wind	10^{-8}	10^{-7}	150	50	10^4	2.6
A5	MHD, light stellar wind, eq. vel.'s	10^{-8}	10^{-7}	100	100	10^4	1.7
A6	MHD, light stellar wind, eq. vel.'s	10^{-8}	10^{-7}	100	100	10^2	1.6

Table 2: Simulation Parameters

3.   Simulation results

3.1.   Density comparisons

We present the results of our simulations in figures 2−7. In figure 2 we present late-time density maps for runs A1, A2, B1 and B2. [3] The intent here is to contrast the case of simultaneous nested winds, with the case of the stellar wind in the absence of the disk wind, for both the MHD, (runs A1 and A2) and HD (runs B1 and B2) cases. Collimation is evident in all four simulations. For the HD cases this is a consequence of the ram pressure of the ambient medium. For the MHD flows, the hoop stresses associated with the toroidal field will also contribute.

The presence of the slower disk wind does not appear to have as significant an effect on the resulting structure of the flow in the case of the hydrodynamic winds. In both cases the stellar wind is refocused toward the axis via the shock at the wind/wind or wind/medium interface over comparable length scales with the focusing length slightly smaller for the case of the single-wind simulation. This small reduction is likely due to the fact that mixing of the disk-wind with the post-shock stellar-wind will impart additional z-directed momentum flux to the flow. Otherwise, the resulting shock structures appear very similar in the hydrodynamic cases.

The differences between the nested-wind and single-wind cases for the MHD cases on the other hand are quite striking. We note first that in the absence of the disk wind, a large rarefied region (a cocoon) opens up along the axis of the wind while a relatively short MHD nose cone evolves at the working surface of the wind shock with several vortices appearing along the bow shock. When both winds operate however, there is considerable mixing between the two flows giving rise to the filimentary structures appearing in the region near the axis in place of rarefaction. In addition, The bow shock has developed a "shoulder," below which an extended and somewhat flattened nose cone protrudes with what appears to be a refocusing event similar to those seen in the hydrodynamic cases occuring in its interior. The shoulder begins to develop early in the simulation soon after the formation of the nose cone and is built up smoothly over the course of the simulation as separate shedding events occurring near the head of the nose cone combine, cool, and expand.

---

[3]The specific run times to which all maps shown in this paper correspond are given for each simulation in table 2.

3.2. Energy maps

We next compare maps of the total energy density to the magnetic energy density, and to maps of plasma-β for both the nested-wind and single-wind cases. Results for the nested-wind case are shown in figure 3 while the single-wind case is presented in figure 4. The top two panels of figure 3 compare total energy density and magnetic energy density for the nested-wind case. We first notice that the map of total energy density is quite similar in appearance to the map of density. This is to be expected since most of the energy in the system is either thermal or kinetic and thus closely traces the density. The map of magnetic energy density has a different appearance. Here we note that in the region bounded on the right by the bow shock "shoulder," the magnetic energy density is distributed in two roughly uniform layers—distinguished by their typical values—throughout the area enclosed and falls off steeply only near the wind/medium interface. The energy densities characteristic of the inner layer are evidently of order $E_{\mathrm{B}} \gtrsim 10^{-6}$ erg cm^{-3} while those of the outer layer are characterized (very roughly) by energy densities in the range $0 \lesssim E_{\mathrm{B}} \lesssim 10^{-10}$ erg cm^{-3}. It is interesting to note that in the extended conical region (an MHD nose cone) to the right of the shoulder, the typical magnetic energy density is of order the highest values found in the *outer* of the two layers to the left of the shoulder. This result is confirmed in the maps of β given in the bottom two panels of figure 3 which indicate values of $\beta \lesssim 1.0$ throughout much of the inner layer while in both the outer layer to the left of the shoulder, and the conical region beyond we find $\beta \gtrsim 10$. Note that in the maps of β, the color black is serving double-duty and indicates very low values of β in the interior of the flow and "infinite" values exterior to it. For this reason we have presented two maps for each simulation; one in which the full range of values of β are mapped, and another "overexposed" map in which values of β are restricted to the range $0 \leq \beta \leq 1$. In this way we are able to show that the very dark interior regions in the panel with unrestricted range are regions of low-β plasma. Note that the magnetic field in the cocoon/bubble is not in fact very strong and does not play an important role in determing the morphology there. This can be seen by examining the plots of β. In the body of the jet downsteam of the interaction region we see that β can be of order 1 and in those regions the field is contributing more significantly to the dynamics.

The noticeable decrease in magnetic energy density in the extended conical region is particularly interesting in light of the observation made earlier of what appears to be the occurance of a hydrodynamic refocusing event in the interior of the extended conical region. These results suggest that while the inertia and over-pressuring of the winds initially lead to an expansion into the ambient medium of the winds, hoop stresses—coupled with the gradual accumulation of shed material—eventually create a bottleneck for the more highly magnetized material in the interior, leading to the ejection of relatively less magnetized material, which then exhibits refocusing similar to the hydrodynamic wind within this extended

region beyond the shoulder.

The single-wind case shown in figure 4 tells a very different story. While the map of total energy density shows some layering indicative of larger energy densities in regions with more material, the magnetic energy is distributed uniformly throughout the region of the flow including in the nose cone at the tip. This is again confirmed in the bottom two panels of figure 4 showing the maps of β for this case.

3.3. Ambient temperature effects

Most of the simulations run for this paper assumed a warm ($T_a = 10^4$ K) ambient medium. Since the type of flows studied here are hypothesized to occur in the non-ionized mediums of post-AGB stars we present in figure 5 the density maps for a pair of nested-wind simulations for the cases of MHD and HD flow respectively with ambient temperature set to $T = 100$ K. The results shown are from runs A3 and B3 in table 1 respectively. We note that in the case of the MHD nested-wind, the same bow shock shoulder, filamentary structures, and extended and flattened nose cone (with some refocusing again evident), are all present in run A3 as well. Comparison with the top panel of figure 2 also indicates that in spite of the now over-pressured jet impinging upon an ambient environment which has had its pressure lowered by two orders of magnitude, the flow suffers very little additional expansion into the medium, suggesting that the hoop stresses play the predominant role in maintaining collimation for the case of MHD nested winds. The hydrodynamic nested-wind on the other hand, suffers a significant amount of expansion when the pressure of the ambient environment is reduced. The rarified region along the axis quadruples its radius and is now bordered by a relatively dense "beam" of material consisting of thoroughly mixed post-shock stellar and disk material, with a characteristic width much greater than the original dimensions of the flow. This layer is in turn bordered by an even denser layer of ambient material plowed up by the flow which, in spite of the shock that forms at its outer edge fails to warm sufficiently to give rise to significant radiative cooling. The resulting appearance is that of an adiabatic wind "piggybacked" upon a radiative wind. This impression is further suggested by the presence of a nose cone near the axis, and a Mach disk above and to its left.

3.4. Effect of mass-loss and velocity variations

It is expected for both the post-AGB and YSO systems that both the stellar and disk winds are expected to have—to order of magnitude—comparable velocities and mass-loss

rates. Still, it is important to investigate how differences in these quantities within the expected range of variation are likely to affect the appearance and physics of the flows. With this in mind we have produced the three simulations for which we present late-time density maps in figure 6. In the top panel of this figure we show the results of run $A4$ in which the velocities of the flows—150 km s^{-1} for the stellar wind and 50 km s^{-1} for the disk wind—are unchanged from our standard run A1, but the mass-loss rate for the stellar wind has been reduced by one order of magnitude relative to the mass-loss rate for the disk wind. Because the temperature of the stellar wind is determined by its velocity and the two parameters σ and β_m, all of which are unchanged from run A1, the effect is to lower the mean density and therefore the pressure of the stellar wind. This allows material from the slower disk wind to expand into, mix with, and disrupt the flow of the stellar wind material, creating a turbulent, filamentary field in the region near the axis which, in run A1 is relatively evacuated.

In the second panel of figure 6 we show results from run A5 in which we have now set the velocities to equal values (100 km s^{-1}). We see that because of the reduced pressure of the stellar wind, the disk wind is still able expand into the region of the stellar wind, and mix with the material there, but because the velocities are equal, this expansion is less disruptive to the flow there. We see a relatively more uniform density field in this region. From comparing these panels to the first of figure 2, in which we also noted the presence of filamentary density structures, we may conclude that differences in both mass-loss rates and flow velocities contribute to determining the degree to which these filamentary density structures arise, and to the characteristic length scales associated with them, in the region of the flow near the axis. In the bottom panel of figure 6, we present the result of run A6 which is identical to run A5 with the exception that the temperature of the ambient medium has been reduced from 10^4 K to 100 K. It is evident in this panel that the effect of this reduction, is to allow for greater expansion of the entire over-pressured flow into the surrounding medium with otherwise little qualitative alteration in the appearance of the flow.

3.5. Mapping the emission

In an attempt to approximate roughly how our interacting winds might appear on the sky, we present in figure 7 synthetic maps of emission for both our nested-wind and single wind cases as obtained in the MHD and HD runs. The intensity shown, which does not distinguish among cooling lines, was determined according to:

$$I_{i,j,k} = \Sigma_k n_{i,j,k}^2 \Lambda(T_{i,j,k}),$$ (10)

where i,j, and k refer to the x,y and z directions in the final data cube created by rotating $n(r, z)$ and $T(r, z)$ about the axis of symmetry, and Λ is the cooling function. A projection angle of $20°$ is assumed in all panels. The left column shows the results for the MHD runs with the nested-winds shown in the top panel and the single-wind shown below. The column on the right shows the corresponding results for the HD case. The maps were generated by revolving the 2.5D data about the axis of symmetry, "tilting" the symmetry axis by a projection angle of $20°$, and subsequently summing along lines of sight and projecting the results on to the image plane. The results are for the total radiative emission. No attempt was made to distinguish among lines of emission. The images show a marked distinction between the MHD and HD cases. While the HD simulations give rise to smooth conical segments of emission which broaden with distance, the MHD results instead give rise to emission divided by primarily on-axis features and ring-like structures centered on the symmetry axis. We also note an interesting difference that appears in the on-axis emission of the nested-winds as contrasted with the stellar-wind case. The emission features on both axes are both quite narrow, but while the on-axis emission for the stellar wind is quite smooth, the corresponding MHD emission shows small but distinct knots of emission distributed along the left half of the axis and vanishing approximately where we earlier noted a bottleneck in magnetic energy arose. While it is possible that the smooth emission seen in both panels could be in part an artifact of the numerical method employed for handling the cylindrical symmetry of the problem, the appearance of the knots in the nested-wind case and their absence in the stellar-wind case suggests that these features are "real." Given that well-aligned knots of emission are routinely observed in optical HH jets, these results, while preliminary, provide cause for asking if these knots of emission are a consequence of interacting nested winds in the environments of YSO's.

The feature that most distinguishes the MHD nested-wind from the other scenarios considered here is the development of the bow shock shoulder mentioned above. This feature was plainly evident in both the warm and cool nested-wind MHD simulations presented here, and would serve as a marker for determining whether an observed object has been formed from simultaneously operating magnetized disk and stellar winds. Before we can robustly employ such a feature as a means of identifying objects as candidates for formation by nested-winds, it will be necessary to study the formation of the shoulder in greater detail. For example, it will be necessary to determine how the formation and appearance of the shoulder varies with such parameters as the disk opening angle, ratios of disk and stellar flow velocities, and ratios of mass-loss rates. (In particular, it is evident from figure 6, that the shoulder is much more subtle in appearance when the mass-loss rate of the star is significantly lower than that of the disk.) But to illustrate what we have in mind, we present as a case in point the Hubble Space Telescope (HST) image of the planetary nebula Hen

2-320 in figure 8. Though other interpretations are possible, the right lobe of this object exhibits features that are qualitatively similar to our MHD nested-wind simulations. We see—indicated by the arrows labeled "shoulders"—an expanded region of the flow nearer to the nebular core, and—indicated by the arrows labeled "nose cones"—a narrower and conical extended region to its right. We also note a brightening of emission at the location where the expanded region gives way to the narrow conical region. This brightening is reminiscent of the large ring of (synthetic) emission seen in the upper-left panel of figure 7 which we note coincides with the location of the bow shock shoulder that arises in this simulation.

4. Discussion and Conclusion

We have presented a series of magnetohydrodynamic (MHD) and hydrodynamic (HD) simulations of the flow arising from the imposition of a simultaneous pairing of nested, steady-state, diverging, interacting, radiative winds on a homogeneous quiescent circumstellar environment. The study was motivated observationally by studies indicating the simultaneous presence of both disk and stellar winds in the environments of proto-planetary nebulae (PPN's), planetary nebulae (PN's) and young stellar objects (YSO's) (Livio 1997 and references therein); and theoretically by the consensus view that disk winds are magnetically launched, and that magnetocentrifugal launch mechanisms acting impulsively over time scales corresponding to the rapid evolution of a poloidally magnetized object are favored to explain the origin of gamma-ray bursts (Piran 2005) and thus—by extension—may plausibly be conjectured to operate in other analogous contexts as well, such as in the environments of the central post-AGB stars associated with PN's and PPN's.

The results of our simulations demonstrate that the physical processes predominantly responsible for maintaining collimation in the outflows differ between the MHD and HD cases, with magnetic hoop stresses being the chief agent of collimation for the MHD runs, while axially-directed refocusing by the shock arising at the wind/environment interface serves a similar purpose in the case of the HD outflows. We also find that the density structures exhibited at late times in the simulations differ significantly both when comparing MHD outflows to HD outflows and when comparing either MHD or HD nested-wind outflows to outflows in which the disk wind is absent. The differences between the nested and single, stellar-wind MHD outflows are the most striking, indicating that the presence of the disk wind has a profound influence on the appearance of both the near-axis regions of the beam and the shape of the bow shock, while the differences between the nested and stellar-wind HD outflows are more subtle showing topologically similar density structure differing mainly in geometric distortions of the bow shock. We have also shown that these results are not

particularly sensitive to differences in temperature of the environment sufficient to distinguish between ionized and un-ionized gas; and that significant disparities in the mass-loss rates parameterizing the stellar versus the disk winds lead to expansion of the denser disk wind material into the region of the stellar wind and the subsequent turbulent disruption of the flow there, and that this effect is most evident when the disk and stellar wind speeds are substantially different.

The work of Akashi 2007, Akashi & Soker 2008 and Akashi et al 2008 bears noting in relation to the present study. In those studies hydrodynamic simulations of a wide jets ($\theta = 30^o$) burrowing into an AGB wind were presented including radiative cooling below 9000K. While magnetic fields were not included in those simulations the results demonstrate the rich variety of features that can be produced in these systems. The results of Akashi and the current study are generally in accord. For example on the issue of temperature in the ambient medium we find that only the MHD runs were relatively unaffected by a change in ambient temperature as one might expect because hoop stresses dominate lateral expansion. The hydrodynamic runs, which are relevant to the Akashi simulations do show significant differences between the cool and hot ambient media in ways that are qualitatively similar to what Akashi saw. It is also noteworthy that Akaski & Soker have been able to create features with protrusions at the head which create the front lobes seen in some PN's without magnetic fields. In MHD the nose cone is a conical region formed when the jet shock stands off at some distance from the bow shock and jet material flowing into the shock does not, effectively, escape into the cocoon. This occurs in MHD jets due to hoop stresses from the toroidal field which restrict the shocked jet gas from radial motion. Akashi & Soker and the current simulations show that conical features at the head of the jet can occur in pure hydrodynamic simulations (though we note it will be a source of confusion to call these nose-cones). We note that further work needs to be done in 3-D in both hydro and MHD to explore the stability of these conical features. Finally we note that the simulations of Akashi & Soker developed dense equatorial rings such as have been observed in some PN and PPN (Hen 2-320). The ability for wide jets to create such features is an attractive feature of the models. In the current simulations we did not observe such dense rings however this is likely a deficiency which occurs due to the size of our inflow region and our choice of a constant density ambient medium. We note that a dense ring was observed to form in the jet/AGB wind models of Garcia-Arrendendo & Frank 2006 where the jet launching region was resolved.

Finally, synthetic maps of emission suggest that fundamentally differing morphologies should be expected between outflows arising from purely HD winds and those arising from MHD winds irrespective of whether both the stellar and disk winds, or just the stellar winds are operating in the environment. They also indicate that when both disk and stellar winds

are operating, knots of emission reminiscent of those seen in the highly collimated optical jets associated with YSO's appear on the axis of symmetry. That these knots are conspicuously absent when only the MHD stellar wind is operating suggests that they may not be an artifact of the axial symmetry imposed by the simulation. This result in particular, points out the need for further work involving fully 3D simulations.

REFERENCES

Akashi, M., & Soker, N. 2008, MNRAS, 391, 1063

Akashi, M., Meiron, Y., & Soker, N. 2008, New Astronomy, 13, 563

Akashi, M., & Soker, N. 2008, New Astronomy, 13, 157

Akiyama, S., Wheeler, J. C., Meier, D. L., & Lichtenstadt, I. 2003, ApJ, 584, 954

Balick, B. 1987, AJ, 94, 671

Balick, B., & Frank, A. 2002, ARA&A, 40,439

Blackman, E. G., Frank, A., Markiel, A.J., Thomas, J.H., & Van Horn, H. M. 2001a, Nature, 409, 485

Blackman, E. G., Frank, A., & Welch, C. 2001b, ApJ, 546, 288

Blackman, E. G., Nordhaus, J. T., & Thomas, J. H. 2006, New Astronomy, 11, 452

Blandford, R. D., & Payne, D. G. 1982, MNRAS, 199, 883

Bujarrabal, V., Castro-Carrizo, A., Alcolea, J., & Sànchez Contreras, C. 2001, A&A, 377, 868

Casse, F., Meliani, Z, Sauty, C. 2007, Ap&SS, 311, 57

Cerqueira, A. H., & de Gouveia Dal Pino, E. M. 1999, ApJ, 510, 828

Cerqueira, A. H., & de Gouveia Dal Pino, E. M. 2001a, ApJ, 550, L91

Cerqueira, A. H., & de Gouveia Dal Pino, E. M. 2001b, ApJ, 560, 779

Contopoulos J, & Lovelace, R. V. E. 1994, ApJ, 429, 139

Cunningham, A. J., Frank, A., Varnière, P., Mitran, S., & Jones, T. W. 2009, ApJS, 182, 519

De Colle, F., & Raga, A. C. 2006, A&A, 449, 1061

de Gouveia Dal Pino, E. M., & Cerqueira, A. H. 2002, RMxAA, 13, 29

Fendt, C. arXiv:0810.415v1 [astro-ph]

Frank, A. 2006, in IAU Symp. 234, Planetary Nebulae in Our Galaxy and Beyond, ed. M. J. barlow & R. H. Mendez (Cambridge: Cambridge Univ. Press), 293

Frank, A., & Blackman, E. G. 2004, ApJ, 614, 737

Frank, A., Ryu, D., Jones, T. W., & Noriega-Crespo, A. 1998 ApJ, 494, L79

Frank, A., Lery, Thibaut, Gardiner, T. A., Jones, T. W., & Ryu, D. 2000, ApJ, 540, 342

Gonçalves, D. R., Corradi, R. L. M., & Mampaso, A. 2001, ApJ, 547, 302

Goodson, A. P., & Winglee, R. M. 1999, ApJ, 524, 159

Kluzniak, W., & Ruderman, M. 1998, ApJ, 505, L113

Lind, K. R., Payne, D. G., Meier, D. L., & Blandford, R. D. 1989, ApJ, 344, 89

Livio, M. 1997, in IAU Coll., 163, Accretion Phenomena and Related Outflows, ed. D. T. Wickramasinghe, G. V. Bicknell, & L. Ferrario, ASP Conf. Ser., 121, 845

Lee, C.-F., Hsu, M.-C., & Sahai, R. 2009, ApJ, 696, 1630

Lee, C.-F., & Sahai, R. 2004, Asymmetrical Planetary Nebulae III: Winds, Structure and the Thunderbird, 313, 465

Lee, C.-F., & Sahai, R. 2004, ApJ, 606, 483

Lee, C.-F., & Sahai, R. 2003, ApJ, 586, 319

Matsakos, T., Tsinganos, K., Vlahakis, N., Massaglia, S., Minogne, A., & Trussoni, E. 2008, A&A, 477, 521

Matt, S., Frank, A., & Blackman, E. G. 2006, ApJ, 647, L45

Meliani, Z., Casse, F., & Sauty, C. 2006, A&A, 460, 1

Nordhaus, J., Blackman, E. G., & Frank, A. 2007, MNRAS, 376, 599

Nordhaus, J., & Blackman, E. G. 2006, MNRAS, 370, 2004

O'Sullivan & Ray 2000, A&A, 363, 355

Pelletier, G. & Pudritz, R. E. 1992, ApJ, 394, 117

Piran, T. 2005, Rev. Mod. Phys., 76, 1143

Pudritz, R. E., & Norman, C. A. 1983, ApJ, 274, 677

Ròżyczka, M., & Franco, J. 1996, ApJ, 469, L127

Sahai, R., & Trauger, J. T. 1998, ApJ, 116, 1357

Shu, F. H., Lizano, S., Ruden, S. P., & Najita, J. 1988, ApJ, 328, L19

Shu, F. H., Najita, J., Ostriker, E., & Wilken, F., Ruden, S., & Lizano, S. 1994a, ApJ, 429, 781

Shu, F. H., & Najita, J., Ruden, S. P., & Lizano, S. 1994b, ApJ, 429, 781

Soker, N. 2004, A&A, 414, 943

Soker, N., & Rappaport, S. 2001, ApJ, 557, 256

Soker, N., & Rappaport, S. 2000, ApJ, 538, 241

Stone, J. M., & Hardee, P. E. 2000, ApJ, 540, 192

Uchida, Y., & Shibata, K. 1985, PASJ, 37, 515

Wheeler, J. C., Meier, D. L., & Wilson, J. R. 2002 ApJ, 568, 807
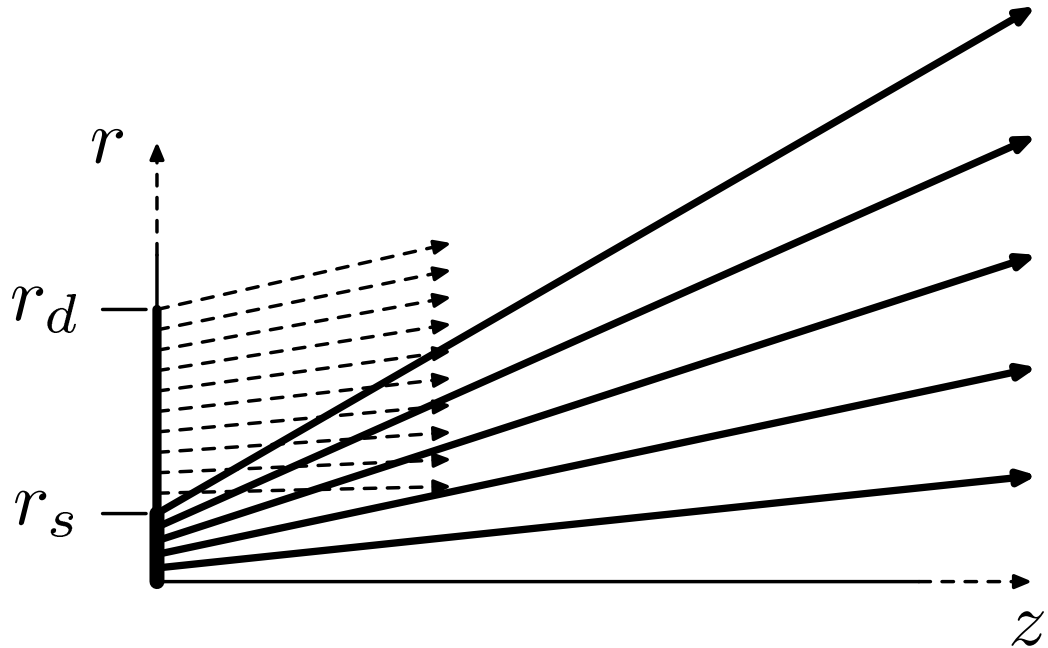
Fig. 1.— Boundary condition for the lower-left corner of the computational domain. The solid arrows represent velocity vectors for the inner wind, while the dashed arrows represent velocity vectors for the disk wind. The outer-most solid arrow makes an angle of 30° with respect to the horizontal axis, while the outer-most dashed arrow makes an angle of 15° with respect to the vertical axis. These values represent the stellar wind opening angle and the disk wind opening angle respectively and are used in all simulations presented in this paper. Also for all simulations we set $r_{\mathrm{d}} = 500$ AU and $r_{\mathrm{s}} = 125$ AU respectively. (See section 2 for a detailed description of the launch region boundary condition.)
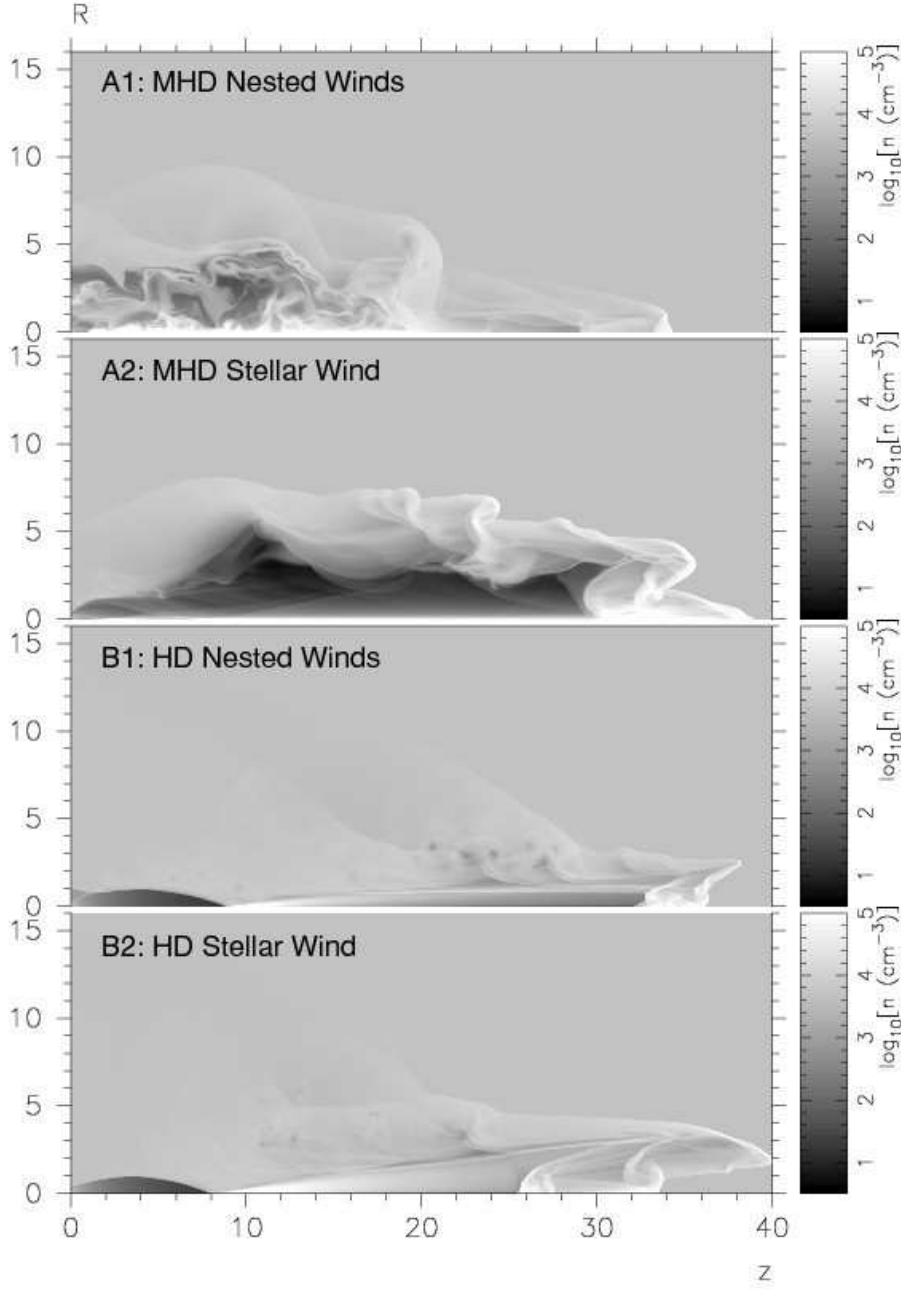
Fig. 2.— Density grey-scales comparing nested-wind simulations to simulations with only a stellar wind for the MHD and HD cases. From top to bottom, the first and second panels show the MHD case with both winds operating and with only the stellar wind operating respectively (runs A1 and A2 in table 1). Similarly, the third and fourth panels show the HD simulations for the case of both winds operating, and with only the stellar wind operating respectively (runs B1 and B2). In all panels, the unit of length is 500 AU and the flow axis is parallel to the image plane.
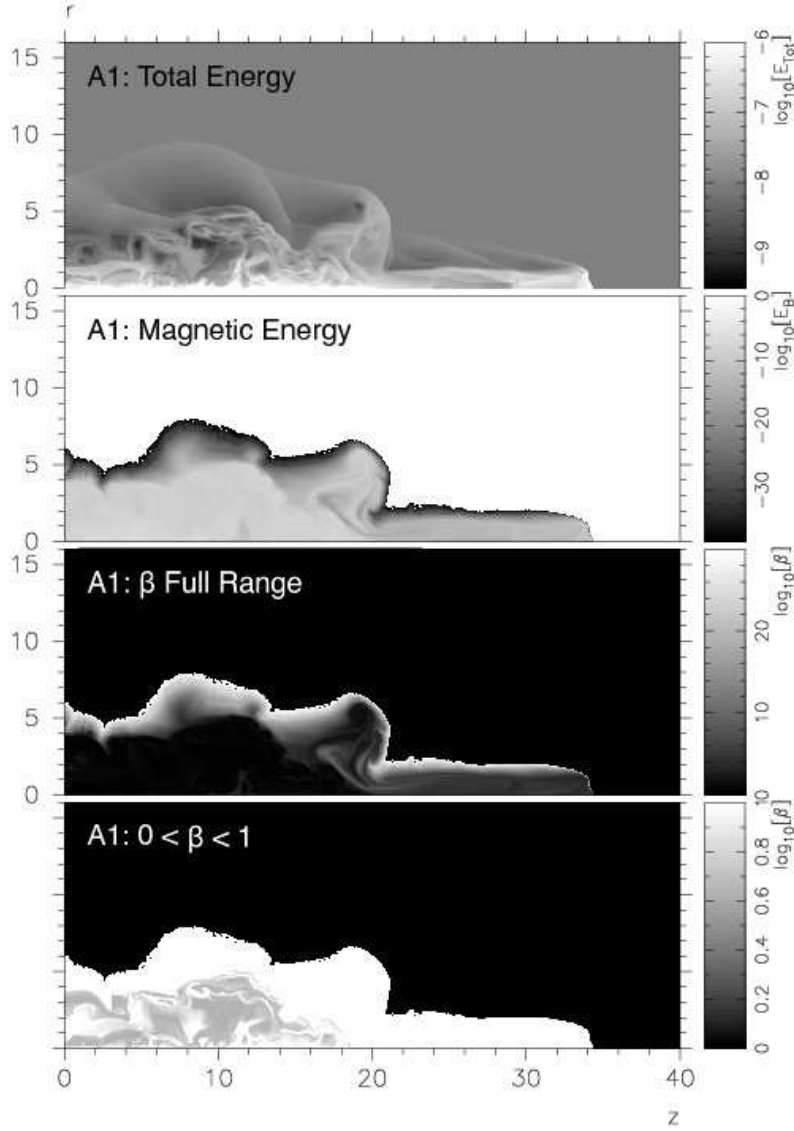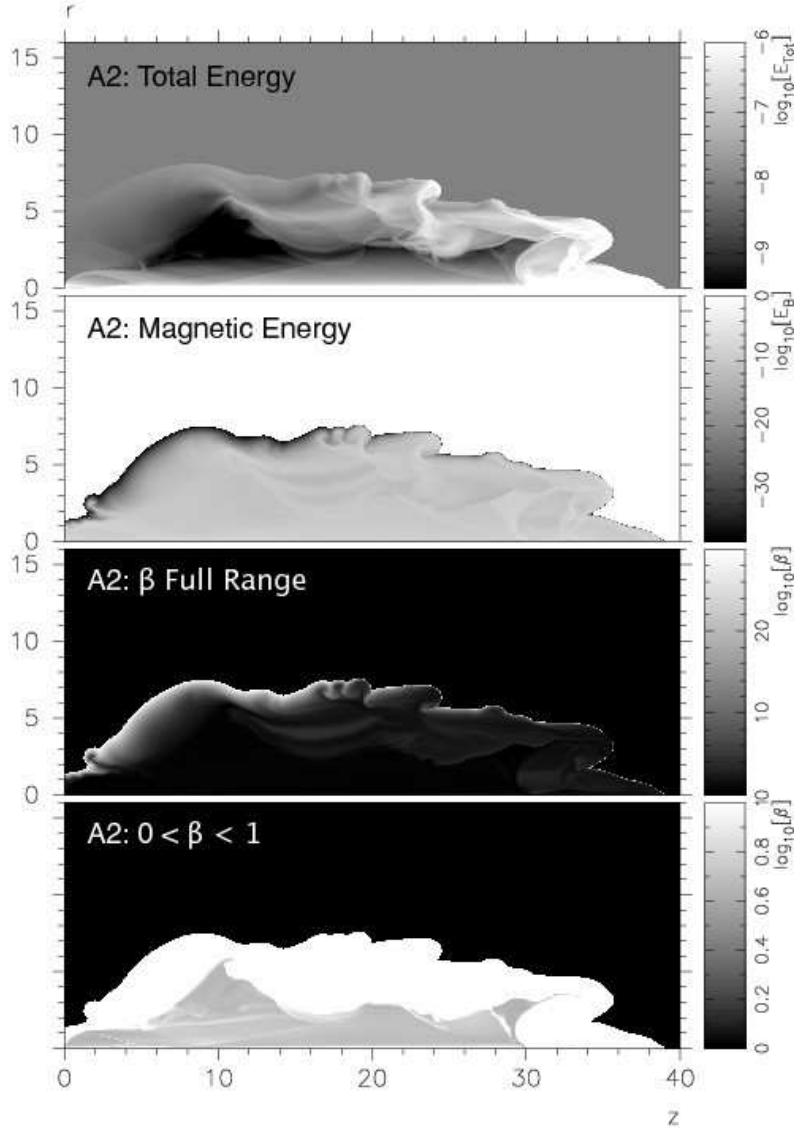
Fig. 3.— Maps of total energy (top panel), magnetic energy (second panel), and plasma-β (bottom two panels) for the MHD nested wind (run A1). For the maps of magnetic energy, the white regions exterior to flow are regions of zero magnetic energy. For visual clarity, two maps of β are given. The third panel, shows the full range of variation in β while the fourth panel shows a map with color-coding restricted to $0 < \beta < 1$ so that details in the variation of β within the beam may be discerned. Pure black regions exterior to the beam have zero magnetic field ($\beta \to \infty$). In all panels the unit of length is 500 AU, and the flow axis is parallel to the image plane.

Fig. 4.— Maps of total energy (top panel), magnetic energy (second panel), and plasma-β (bottom two panels) for the MHD single wind (run A2). For the maps of magnetic energy, the white regions exterior to flow are regions of zero magnetic energy. For visual clarity, two maps of β are given. The third panel, shows the full range of variation in β while the fourth panel shows a map with color-coding restricted to $0 < \beta < 1$ so that details in the variation of β within the beam may be discerned. Pure black regions exterior to the beam have zero magnetic field ($\beta \to \infty$). in all panels the unit of length is 500 AU and the flow axis is parallel to the image plane.
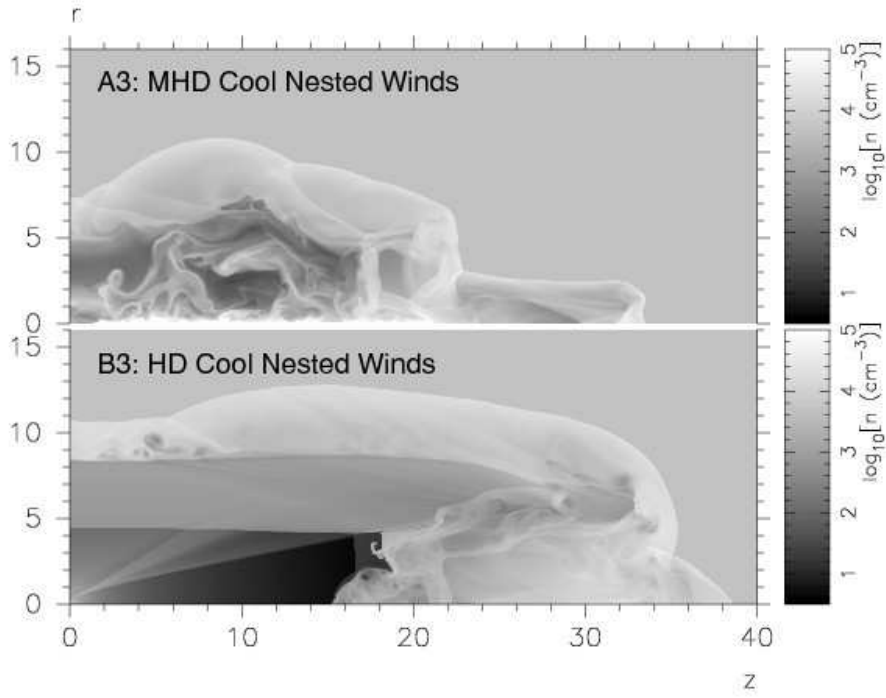
Fig. 5.— Comparison of MHD (top panel) and HD (bottom panel) nested wind flows for the case of a cool,($T_a = 100K$), ambient medium. Both stellar and disk winds operate for both of the cases shown, (runs A3 and B3 respectively). In both panels the unit of length is 500 AU and the flow axis is parallel to the image plane.
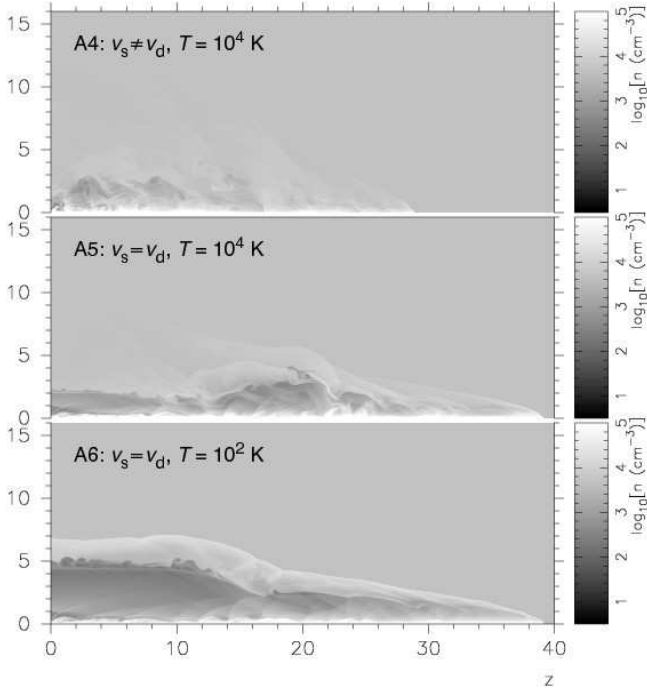
Fig. 6.— Density maps of MHD nested winds for the case of a "light" stellar wind. The maps shown correspond, from top to bottom, to runs A4, A5, and A6, respectively (See table 1). In all panels the unit of length is 500 AU and the flow axis is parallel to the image plane.
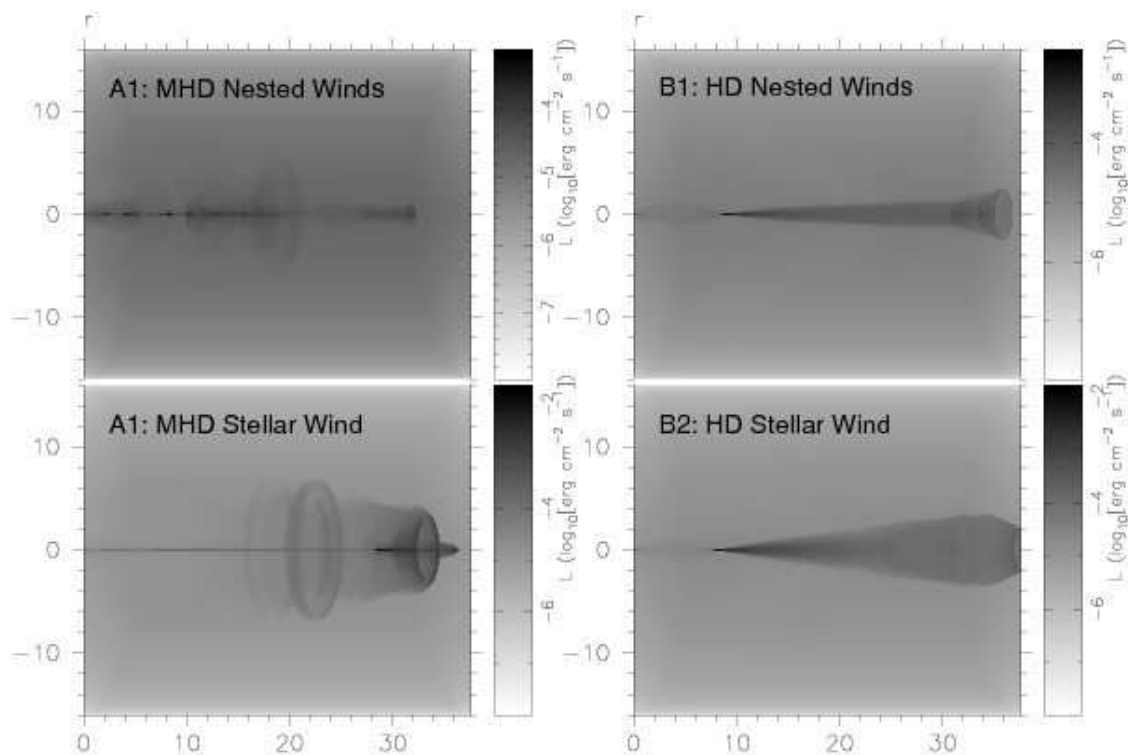
Fig. 7.— Synthetic maps of radiative emission for nested and single wind simulations. The panels in the left column of the figure are from the MHD nested wind (top) and stellar winds (bottom) respectively (runs A1 and A2). The panels in the right column are from the HD nested (top) and stellar (bottom) winds respectively (runs B1 and B2). In all panels the unit of length is 500 AU and the flow axis makes a 20° angle with respect to the image plane.
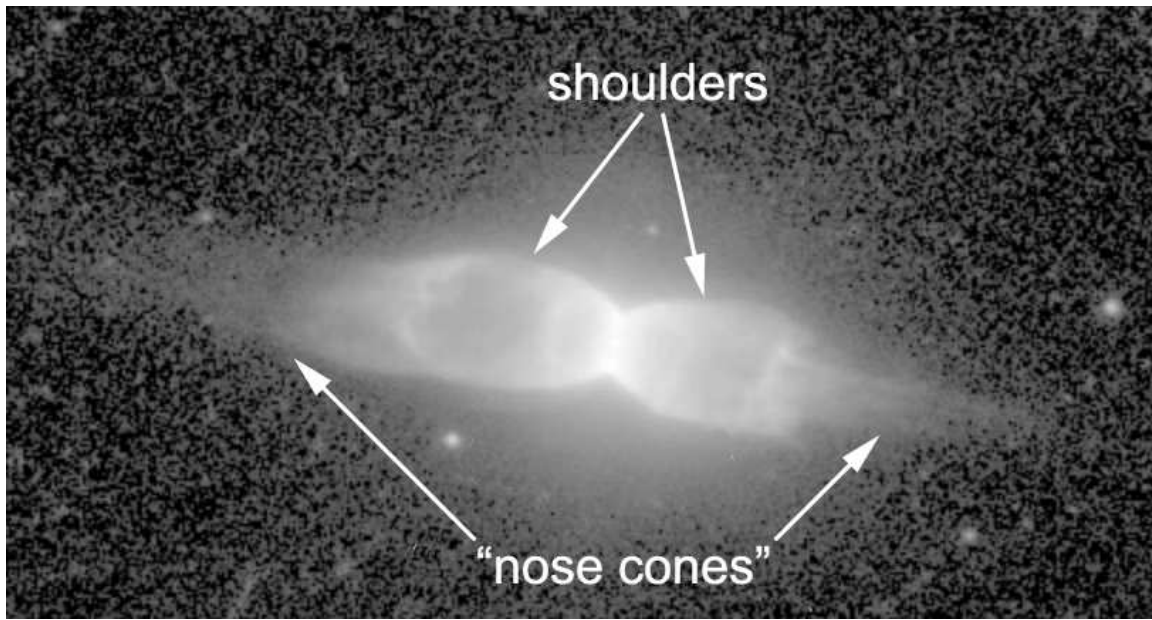
Fig. 8.— An image of Hen 2-320 taken with the HST/WFPC2/PC camera through the F659N filter and displayed logarithmically (credit: NASA and HST proposal GO8345, R. Sahai, P.I.). See section 3 for a discussion of the identified features."